

**John Pearce<sup>1</sup>**

Department of Electrical and  
Computer Engineering,  
The University of Texas at Austin,  
Austin, TX 78712  
e-mail: jpearce@mail.utexas.edu

**Andrew Giustini**

Thayer School of Engineering,  
Dartmouth College,  
Hanover, NH 03755;  
Geisel School of Medicine,  
Dartmouth College,  
Hanover, NH 03755

**Robert Stigliano**

Thayer School of Engineering,  
Dartmouth College,  
Hanover, NH 03755

**P. Jack Hoopes**

Thayer School of Engineering,  
Dartmouth College,  
Hanover, NH 03755;  
Geisel School of Medicine,  
Dartmouth College,  
Hanover, NH 03755

# Magnetic Heating of Nanoparticles: The Importance of Particle Clustering to Achieve Therapeutic Temperatures

*Hyperthermia therapy for cancer treatment seeks to destroy tumors through heating alone or combined with other therapies at elevated temperatures between 41.8 and 48 °C. Various forms of cell death including apoptosis and necrosis occur depending on temperature and heating time. Effective tumoricidal effects can also be produced by inducing damage to the tissue vasculature and stroma; however, surrounding normal tissue must be spared to a large extent. Magnetic nanoparticles have been under experimental investigation in recent years as a means to provide a favorable therapeutic ratio for local hyperthermia; however, practical numerical models that can be used to study the underlying mechanisms in realistic geometries have not previously appeared to our knowledge. Useful numerical modeling of these experiments is made extremely difficult by the many orders of magnitude in the geometries: from nanometers to centimeters. What has been missing is a practical numerical modeling approach that can be used to more deeply understand the experiments. We develop and present numerical models that reveal the extent and dominance of the local heat transfer boundary conditions, and provide a new approach that may simplify the numerical problem sufficiently to make ordinary computing machinery capable of generating useful predictions. The objectives of this paper are to place the discussion in a convenient interchangeable classical electromagnetic formulation, and to develop useful engineering approximations to the larger multiscale numerical modeling problem that can potentially be used in experiment evaluation; and eventually, may prove useful in treatment planning. We cast the basic heating mechanisms in the framework of classical electromagnetic field theory and provide calibrating analytical calculations and preliminary experimental results on BNF-Starch<sup>®</sup> nanoparticles in a mouse tumor model for perspective. [DOI: 10.1115/1.4024904]*

## 1 Introduction

Magnetic iron oxide nanoparticles (mNP), magnetite and maghemite, are under investigation as a means to provide a favorable therapeutic ratio for local hyperthermia treatment of tumors, and to make localized heating of the tumor less engineering-intensive and more cancer cell specific. They have been used successfully to localize tumor heating in experimental animals and in vitro [1–10]. Heating of nanoparticles is complicated by the short thermal relaxation time constants and difficulty of coupling sufficient power to achieve desired temperatures without creating toxic eddy currents in the tissues. Rabin [11] argues convincingly that individual (i.e., dispersed) nanoparticles are not able to effectively heat cells and tissues in electromagnetic fields because their small size results in extremely short thermal time constants, and the power densities required are too high to be practical. Nevertheless, experimental evidence shows that sufficient nanoparticle heating can be achieved with the same magnetic nanoparticles if spatially appropriate aggregates of NPs can be achieved; but clustering of the particles is essential to achieve useful results [5,12].

Magnetic field heating of iron oxide nanoparticles is typically accomplished by the hysteresis loop mechanism in alternating magnetic fields (AMFs), either due to Néel relaxation, Brownian motion, or perhaps, particle–particle interaction in super-paramagnetic nanoparticles at frequencies between 100 and 300 kHz, and has proven to be effective. The precise mechanism

is somewhat controversial at this point, since it has not been clearly delineated and may consist of a combination of these, and perhaps other, mechanisms. In all cases the heating field is highly local in nature, and effective treatment depends on clustering and the spatial distribution of particles in strategically advantageous locations.

To date almost all of the germane literature has been confined to experimental studies; the single exception that we have been able to identify is the work of Etheridge and Bischof, which included experiments and numerical models of suspended mNPs in a droplet [13]. Finite element method (FEM) numerical models can also be used to estimate the order of magnitude of volume power density,  $Q_{\text{gen}}$  ( $\text{W m}^{-3}$ ) required to achieve significant heating in evenly dispersed and aggregated clusters of nanoparticles in more realistic multiple heat transfer and tumor geometry environments, which was one of the goals of this study. The FEM models developed in this study were confined to continuum formulations and did not include film nano-dimension heat transfer effects at the nanoparticle surface. The models illustrate the overwhelming effect of local heat transfer processes and the multiscale nature of the root problem. We develop and implement approximate numerical model approaches that illuminate the relative importance of biodistribution of mNPs and the local heat transfer boundary conditions. The results make practical ordinary sized FEM models of larger geometries and should facilitate the eventual engineering design and analysis of nanoparticle heating in realistic tumor-sized systems. While tumor-sized model spaces have not yet been developed, the pathway to do so is identified and described.

<sup>1</sup>Corresponding author.

Manuscript received November 2, 2012; final manuscript received June 10, 2013; published online July 16, 2013. Assoc. Editor: Malisa Samtinoranont.

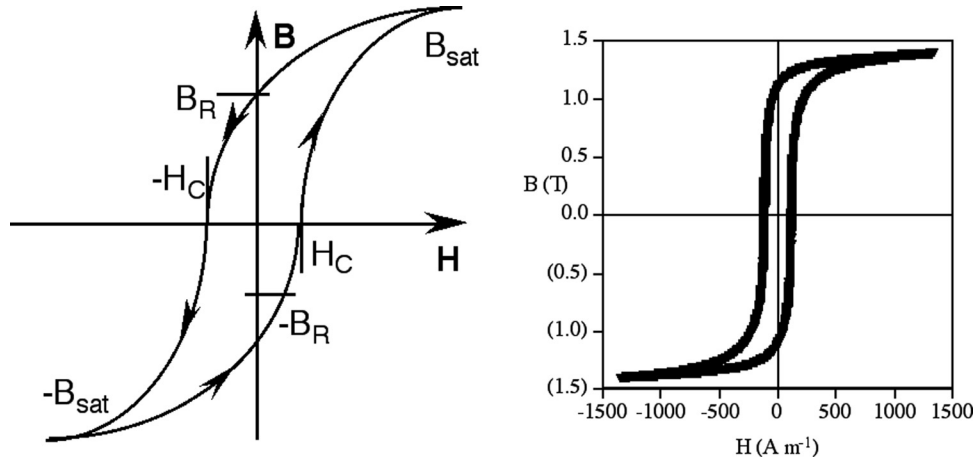


**Fig. 1** (a) Hysteresis loop in the B-H curve indicates losses. (b) Measured B-H curve at 1 kHz in a 3% Silicon iron alloy (with a small amount of Al and trace of C), generically referred to as 3SiFe.  $B_R = 1.1$  (T) and  $H_C = 114$  (A m<sup>-1</sup>) in this material. Plot data kindly provided by Dr. Aleta Wilder.

## 2 Methods

Translating the governing electromagnetic relations into formulations suitable for analyzing experimental data, and predicting heating results in numerical models takes on different forms for

the modalities applied to date. FEM numerical models of mNP heating were constructed using COMSOL 3.5a (Comsol, Inc. Burlington, MA). Two numerical model series were executed assuming uniform NP heating in the magnetic field: uniformly dispersed individual NPs, and NP clusters of varying size in

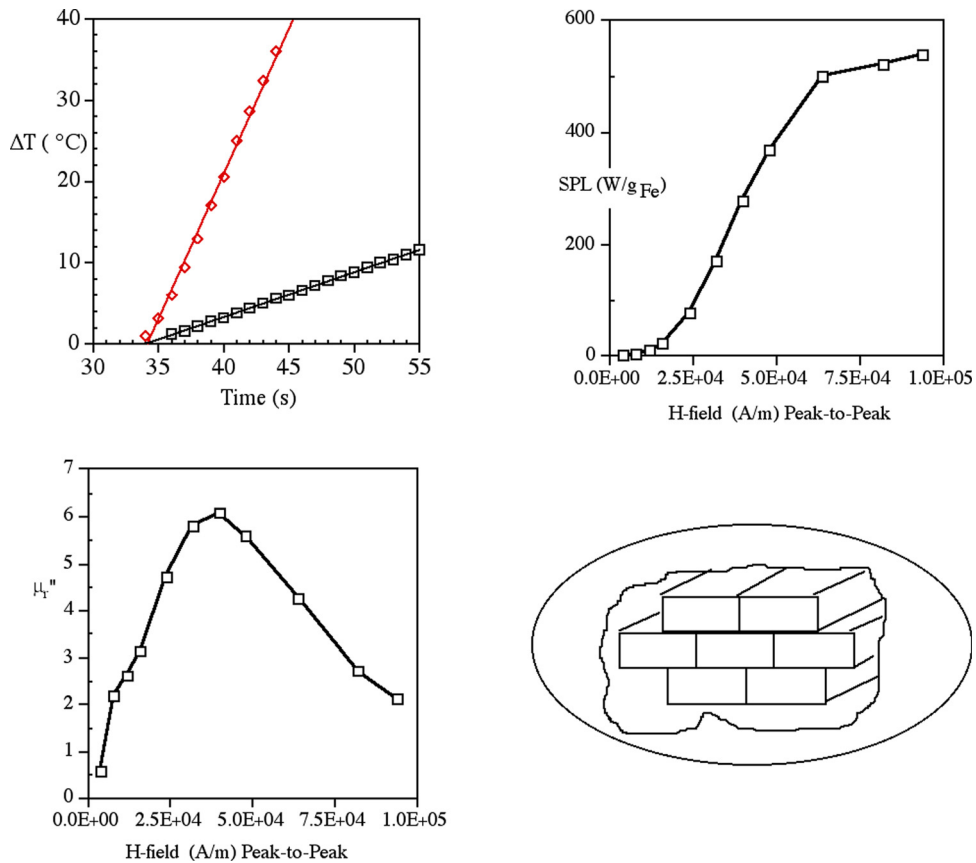


**Fig. 2** (a) Heating rate in BNF-Starch<sup>®</sup> (MicroMod 100-00-102), magnetic nanoparticles (Fe<sub>3</sub>O<sub>4</sub>) in solution at 150 kHz in applied magnetic fields of  $H = 24$  (kA m<sup>-1</sup>) and  $90$  (kA m<sup>-1</sup>)—300 and 1130 Oe, respectively [14]. (b) SPL versus applied H-field (in peak-to-peak A m<sup>-1</sup>) for BNF-starch solution. (c) The imaginary relative permeability,  $\mu''$ , versus applied H-field (in peak-to-peak A m<sup>-1</sup>). (d) Figurative sketch of the structure of a BNF-starch particle. The magnetic material consists of  $6.5 \times 19 \times 49$  nm parallelepiped shaped magnetite crystals closely packed into what is effectively a single suspended solid, nominal particle. The coated particle's hydrodynamic diameter is 100 nm [16].

single- and multiple-cell sized model spaces. Some analysis is necessary to convert the typical formulations into a form suitable for the numerical model governing equations, and to estimate the order of magnitude of volume power generation that is achievable in typical experiments.

## 2.1 Physical Bases for the Calculations

**2.1.1 Energy Balance.** The governing energy balance equation is a reduced form of the bio-heat equation and is necessarily in reduced form for NP heating because the nanoparticles are extremely small with respect to the dimensions that characterize conventional perfusion and blood flow mechanisms

$$\rho_t c_t \frac{\partial T}{\partial t} = \nabla \cdot (k \nabla T) + Q_{\text{gen}} + Q_{\text{met}} \quad (1)$$

where:  $\rho$  = density ( $\text{kg m}^{-3}$ ),  $c$  = specific heat ( $\text{J kg}^{-1} \text{K}^{-1}$ ),  $k$  = thermal conductivity ( $\text{W m}^{-1} \text{K}^{-1}$ ),  $Q_{\text{gen}}$  = volumetric power density ( $\text{W m}^{-3}$ ), and  $Q_{\text{met}}$  = metabolic heat ( $\text{W m}^{-3}$ ). The “t” subscript is generically “tissue,” that collectively describes both cytosolic and extra-cellular components.

**2.1.2 Electromagnetic Heating.** In an electromagnetic field, the volumetric power density,  $Q_{\text{gen}}$ , is the real part of the divergence of the Poynting Vector,  $\mathbf{S}$ , where in the complex plane  $\mathbf{S} = \mathbf{E} \times \mathbf{H}^*$  ( $\text{W m}^{-2}$ ) is the power density in the electromagnetic field,  $\mathbf{E}$  is the vector electric field ( $\text{V}_{\text{rms}} \text{m}^{-1}$ ), and  $\mathbf{H}^*$  is the complex conjugate of the vector magnetic field ( $\text{A}_{\text{rms}} \text{m}^{-1}$ )

$$\begin{aligned} -\oint_{\Sigma} \mathbf{S} \cdot d\mathbf{A} &= -\oint_{\Sigma} \mathbf{E} \times \mathbf{H} \cdot d\mathbf{A} \\ &= \iiint_{\text{vol}} [\mathbf{E} \cdot \mathbf{J} + \mathbf{E} \cdot j\omega \mathbf{D} + \mathbf{H} \cdot j\omega \mathbf{B}] dv \end{aligned} \quad (2)$$

In this relation,  $\Sigma$  is a closed surface with surface normal,  $d\mathbf{A}$  ( $\text{m}^2$ ), and “vol” is the volume enclosed by  $\Sigma$ . Because the frequency domain has been used the electromagnetic fields are sinusoidal.

The negative sign on the left hand side of the Poynting Power Theorem, Eq. (2), indicates that power is absorbed from the electromagnetic field. By the divergence theorem, at every point in the field

$$-\nabla \cdot \mathbf{S} = (\sigma + j\omega\epsilon^*)|\mathbf{E}|^2 + j\omega\mu^*|\mathbf{H}|^2 \quad (3)$$

and the constitutive relations have been substituted— $\sigma$  = electrical conductivity ( $\text{S m}^{-1}$ ),  $\epsilon^*$  = complex electric permittivity ( $\text{F m}^{-1}$ ), and  $\mu^*$  = complex magnetic permeability ( $\text{Hy m}^{-1}$ ). Both the permittivity and permeability are complex in sinusoidal fields:  $\epsilon^* = \epsilon' - j\epsilon''$  ( $\text{F m}^{-1}$ ) and  $\mu^* = \mu' - j\mu''$  ( $\text{Hy m}^{-1}$ ), with the real part describing stored energy and the imaginary part dissipated energy. The imaginary parts of  $\epsilon^*$  and  $\mu^*$  are always negative because materials are causal: i.e., they cannot anticipate the application of a field. Electric and magnetic dipole rotational motion losses that result in heating are described by the imaginary part of the applicable physical properties and the divergence is

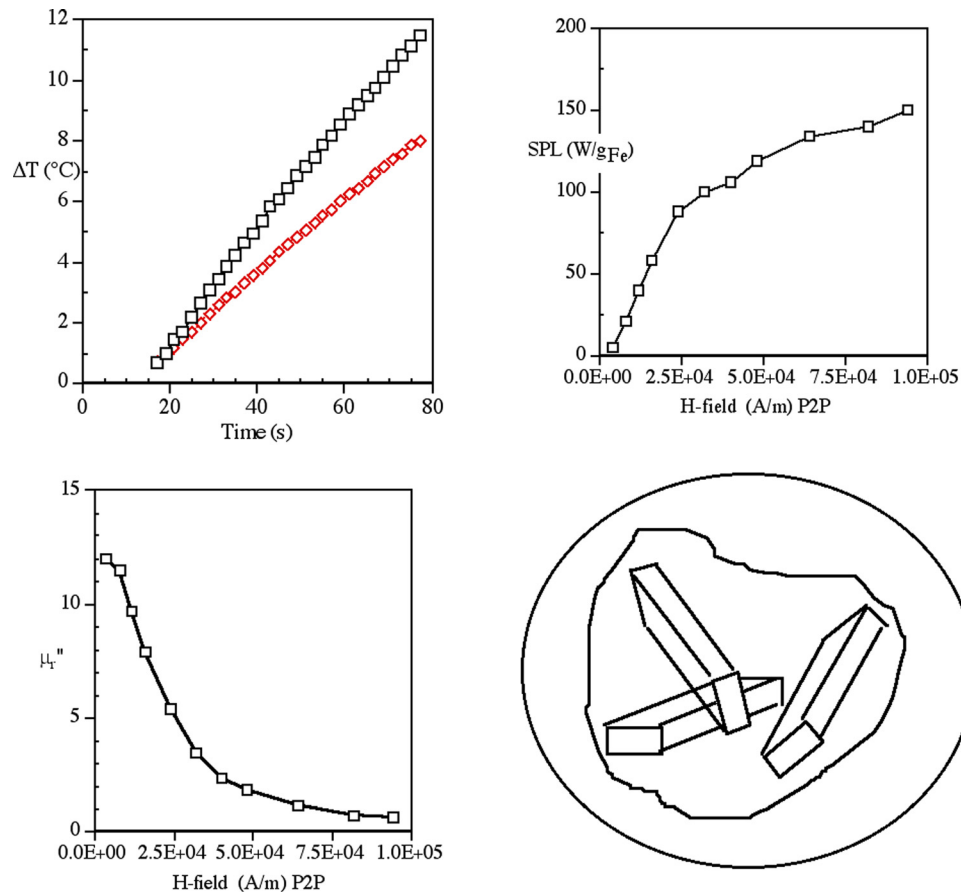


**Fig. 3** (a) Heating rate in “nanomag-D-sprio<sup>®</sup>” super-paramagnetic nanoparticles ( $\text{Fe}_3\text{O}_4$ ) solution at 150 kHz in applied magnetic fields of  $H = 24 \text{ (kA m}^{-1}\text{)}$  and  $64 \text{ (kA m}^{-1}\text{)}$ —300 and 800 Oe, respectively [14]. (b) SPL versus applied H-field for BNF-starch (in peak-to-peak  $\text{A m}^{-1}$ ). (c) The relative imaginary permeability,  $\mu_r''$  (no units). (d) Figurative sketch of the individually suspended magnetic nanoparticles [16].

therefore complex, with the imaginary part describing the stored energy, and the real part the power dissipated at a point

$$Q_{\text{gen}} = \text{Re}\{-\nabla \cdot \mathbf{S}\} = (\sigma + \omega\epsilon'')|\mathbf{E}|^2 + \omega\mu''|\mathbf{H}|^2 \quad (4)$$

Magnetic field heating is accomplished by two typical mechanisms: Joule heating and magnetic field absorption. Joule heating from magnetic field induction—eddy current generation by Faraday's Law—occurs when free semi-conducting charge carriers (ions in tissues) collide with other charge carriers or with the “lattice”—other atoms and molecules in the tissue—dissipating energy. Magnetic field heating mechanisms include relaxation losses in magnetic dipoles (Néel relaxation) within a particle as the magnetic dipole moment oscillates, and motional dissipation, due to Brownian motion of particles in response to a time-varying magnetic field. It is also possible that particle–particle interaction between individual iron oxide particles suspended in a larger

starch coating, such as in the super-paramagnetic iron oxide (SPIO), mNPs, may contribute an additional mechanism. For the apparently dominant hysteresis loop mechanism  $Q_{\text{gen}} = \omega\mu'' |\mathbf{H}|^2$  ( $\text{W m}^{-3}$ )  $\simeq \omega B_R H_C$ —i.e.,  $Q_{\text{gen}} \simeq \omega B_R H_C$ , where  $B_R$  is the remanence (at  $\mathbf{H}=0$ ) and  $H_C$  the coercivity (at  $\mathbf{B}=0$ ). This estimate assumes that the material is approximately “square,” i.e., that the hysteresis loop can be modeled as essentially rectangular. Measured hysteresis loops are generally curvilinear, as sketched in Fig. 1(a) and plotted in Fig. 1(b).

**2.2 Practical Formulation of Magnetic Nanoparticle Heating.** Quantitative values of  $Q_{\text{gen}}$  that can be used in these calculations are not common in literature on the topic of iron oxide nanoparticles. The underlying reasons for this are many, but in some sense originate in the formulation of magnetic field equations in cgs units. SI units are much preferred for many reasons, and we translate some of the recent literature into them to

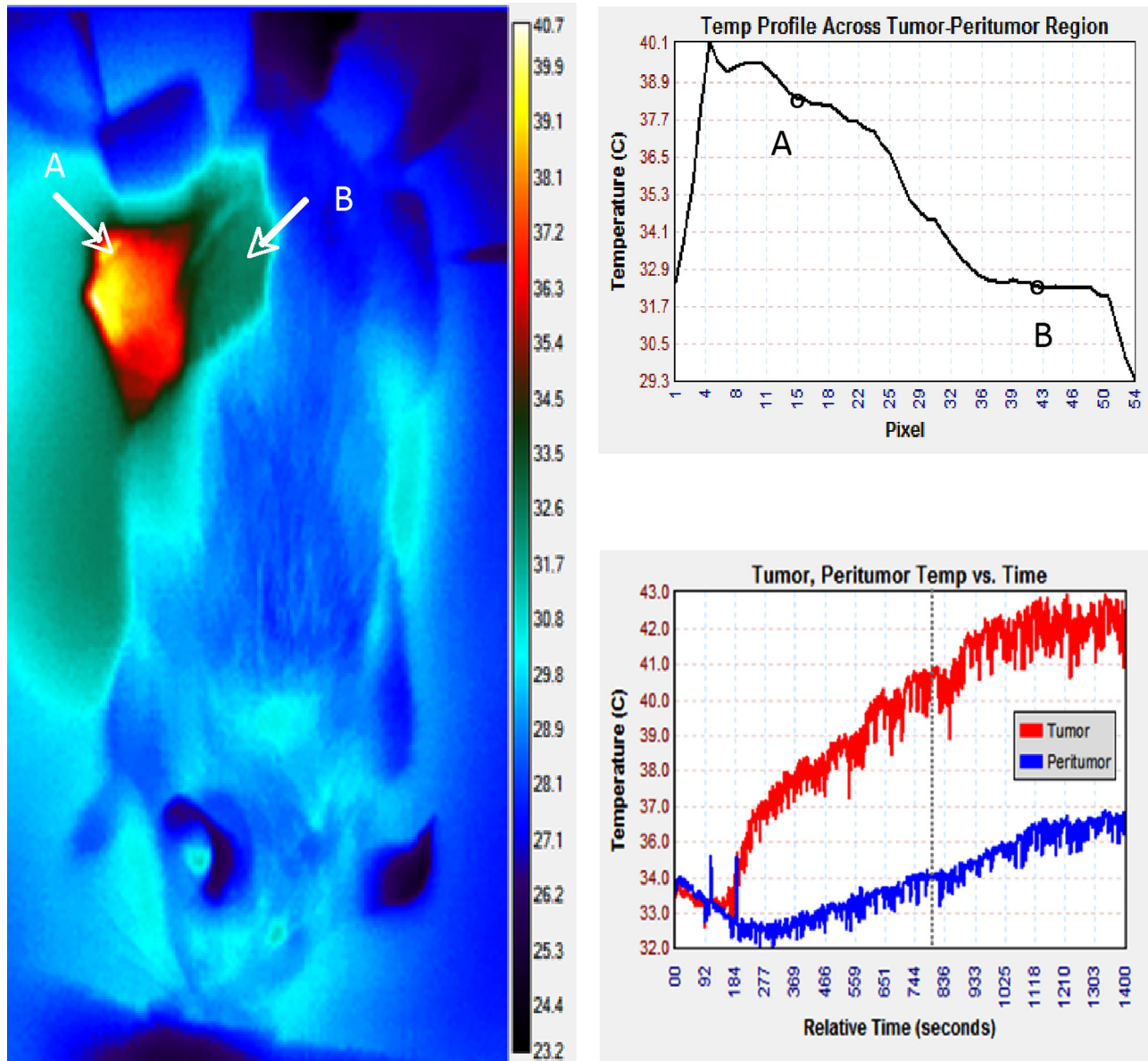


Fig. 4 Magnetic nanoparticle treatment of a murine breast cancer tumor implanted on the flank. (a) Thermal camera image of a mouse during treatment. The bare skin of the tumor (left arrow) and peritumor, adjacent noncancerous tissue (right arrow), are marked. (b) Surface temperature profile across the area of interest, including tumor and nontumor tissue. The temperature distribution along a straight line intersecting points A and B is shown. (c) Maximum recorded surface temperature of tumor and peritumor areas are plotted versus time (recorded at 1 frame/s).



facilitate quantitative analysis. Further, the majority of experimental measurements on heating rate,  $dT/dt$ , have been conducted in closely packed nanoparticles at volume fractions unachievable in realizable biodistributions.

**2.2.1 Hysteresis Loop Heating.** Practical data collection is often limited to measuring temperature rise in carefully constructed magnetic field calorimeters [14]. The hysteresis loop is maximally open at specific frequencies. When saturation occurs the permeability is nonlinear, complex ( $\mu'' > 0$ ) and not constant with applied field strength [14]. If the cyclic magnetic field strength does not saturate the medium to some degree, hysteresis is not observed, and the permeability is essentially real ( $\mu'' = 0$ ) and constant. In Fig. 2, the reported work of Bordelon et al. [14], 100 nm  $\text{Fe}_3\text{O}_4$  BNF-Starch<sup>®</sup> magnetic nanoparticles (MicroMod, Partikeltechnologie, GmbH, Rostock, Germany) coated with hydroxyethyl starch (with water as the solvent) were heated at 150 kHz in magnetic fields of 24 and 90 ( $\text{kA m}^{-1}$ ) peak-to-peak (300 and 1125 Oe). These two applied H-fields have heating rates of 0.555 and  $3.62$  ( $^\circ\text{C s}^{-1}$ ), respectively (linear regression lines as shown with  $r^2 = 1.000$  and  $0.996$ , respectively), as in Fig. 2(a). These NPs are nominally 100 nm in hydrodynamic diameter containing multiple 15–20 nm iron oxide crystals—the particle concentration was 44 ( $\text{mg ml}^{-1}$ ) with an iron concentration of 29.1 ( $\text{mg ml}^{-1}$ ) [14]. We have also used these mNPs in experimental studies reported elsewhere [5]. It should be noted that because of the eddy current heating mechanism, magnetic field strengths above about  $24 \text{ kA m}^{-1}$  (300 Oe) are likely to prove practical only in relatively small regions of highly focused heating in vivo.

Bordelon et al. derived specific power loss (SPL) correlates from the rate of temperature rise experiments, as in Fig. 2(a), in a calorimeter; where the specific power loss ( $\text{W g}^{-1}\text{Fe}$ ) is derived from the early stage of the heating

$$\text{SPL} = \left( \frac{1}{m_{\text{Fe}}} \right) c \left[ \frac{\Delta T}{\Delta t} \right]_{t \rightarrow 0} \quad \text{therefore} \quad \mu_r'' \mu_0 = \frac{\rho_{\text{Fe}} \text{SPL}}{\omega |\mathbf{H}|^2} \quad (5)$$

where:  $m_{\text{Fe}}$  is the mass of iron, the temperature rise is measured under essentially adiabatic conditions,  $c$  = specific heat of the suspension (dominated by the water solvent),  $\mu_r''$  is the imaginary part of the relative permeability,  $\rho_{\text{Fe}}$  is the density of iron oxide,  $\sim 5.18 \times 10^6$  ( $\text{g m}^{-3}$ ) in this calculation, and since it is a power calculation,  $H$  is converted from peak-to-peak to rms ( $\text{A}_{\text{rms}} \text{m}^{-1}$ ). Bordelon et al. noted that the SPL does not precisely follow the expected dependence on applied magnetic field strength, Fig. 2(b) (data from Table III in their paper) [14]. Comparing to Eq. (4), we would expect that the imaginary part of the relative permeability,  $\mu_r''$ , should be relatively constant; however, in their measurements  $\mu_r''$  varies from 0.57 to 6.08, as in Fig. 2(c). This is clear evidence of nonlinear behavior in the material that is most likely due to opening in the hysteresis loop.

**2.2.2 Magnetic Dipole Relaxation in Super-Paramagnetic Iron Oxide.** Magnetic nanoparticles are classified as super-paramagnetic when their hysteresis loop, measured under quasi-static conditions, has zero loop area. This occurs when the nanoparticle cores are small enough to support only one magnetic domain per core (single domain particles). Super-paramagnetic response in the magnetic dipoles occurs above the Curie point temperature in bulk materials, where the magnetic spins are randomly oriented: these materials do not have a net magnetic dipole moment. Nanometer dimension particles smaller than approximately 50 nm are single domain, meaning that no magnetic grain boundaries exist within [15]. Small iron oxide nanoparticles are therefore classed as “super-paramagnetic” because they exhibit the characteristic random polarization much below their Curie point temperature.

The super-paramagnetic iron oxide (nanomag-D-spio<sup>®</sup>) nanoparticles are small enough that individual grain boundaries do not form, and are thus super-paramagnetic below the bulk material

Curie point [16]. Additionally, rather than being forged into a single bar, they are suspended in the coating medium, and can thus interact with each other under applied magnetic fields—a form of “transient dipole/induced dipole” interaction.

The maximum dimensions at which nanoparticles transition to super-paramagnetic behavior is a matter of some discussion. Hergt et al. [17] quote 20 nm, which value was used by Etheridge and Bischof [13] in their work. Brosseau et al. [15] suggest 100 nm for the grain formation lower limit. Bordelon et al. use 50 nm [14].

When an AMF is applied, these particles are dominated by one of two relaxation mechanisms, Néel relaxation or Brownian relaxation. Néel relaxation heating occurs when the magnetic dipole of a single domain particle spontaneously reverses direction in response to an applied magnetic field. Brownian relaxation heating occurs when particles physically rotate to align their magnetic dipole with an applied magnetic field, without a reversal of the magnetic dipole occurring [18,19]. The effective relaxation time of a noninteracting single domain magnetic particle will be dominated by the mechanism exhibiting the shortest relaxation time for that particle. As described by Rosensweig [19], Hergt et al. [20], and others, the Brownian relaxation time,  $\tau_B$ , is described by

**Table 1 Thermal properties common to the numerical models**

Material	$k$ ( $\text{W m}^{-1} \text{K}^{-1}$ )	$\rho$ ( $\text{kg m}^{-3}$ )	$c$ ( $\text{J kg}^{-1} \text{K}^{-1}$ )
Cytosol	0.5	1050	3700
Nucleus	0.5	1050	3700
Dextran	0.614	1430	1260
Iron oxide	3.85	5180	641.5

**Table 2 Summary of FEM numerical model results**

Single cell models			
Uniform distribution, $10^{13}$ (NP ml <sup>-1</sup> )			
NP diameter (nm)	$Q_{\text{gen}}$ (W m <sup>-3</sup> )	$T_{\text{particle}}$ (°C)	
36	$1 \times 10^{16}$	52	
50	$1 \times 10^{16}$	72	
80	$1 \times 10^{15}$	50	
Single NP clusters			
No. of NPs, 50 nm diameter	$Q_{\text{gen}}$ (W m <sup>-3</sup> )	$T_{\text{particle}}$ (°C)	
5	$3 \times 10^{16}$	55	
19	$1 \times 10^{16}$	50	
45 in 2 layers	$3 \times 10^{15}$	44	
90 in 4 layers	$3 \times 10^{15}$	49	
180 in 2 layers	$1 \times 10^{15}$	42	
Multiple equivalent ellipsoids			
No. of ellipsoids	Equivalent NPs	$Q_{\text{gen}}$ (W m <sup>-3</sup> )	$T_{\text{max}}$ (°C)
1	90	$3 \times 10^{15}$	59.5
8 in 2 layers	1980	$1.5 \times 10^{14}$	45
1	81,000	$3 \times 10^{11}$	48.6
Multiple cell models			
No. of cells/NPs	Distance between isothermal boundaries (μm)	$Q_{\text{gen}}$ (W m <sup>-3</sup> )	$T_{\text{max}}$ (°C)
4/7920 NPs	80	$1 \times 10^{14}$	59
4/76,000 NPs	160	$3 \times 10^{10}$	42.8
8/15,840 NPs	160	$1 \times 10^{13}$	45

Eq. (6a), the Néel relaxation time,  $\tau_N$ , by Eq. (6b), and the effective relaxation time constant,  $\tau$ , Eq. (6c)

$$\tau_B = \frac{\pi \eta d_h^3}{2kT} \quad (6a)$$

$$\tau_N = \tau_0 e^{\frac{KV}{kT}} \quad (6b)$$

$$\tau = \frac{\tau_N \tau_B}{\tau_N + \tau_B} \quad (6c)$$

where:  $\eta$  = viscosity (Pa s),  $d_h$  = hydrodynamic diameter (m),  $k$  = Boltzmann's constant ( $J K^{-1}$ ),  $T$  = temperature (K),  $\tau_0 \approx 10^{-9}$  (s), and  $KV$  = the anisotropy energy (an activation barrier, where  $K \sim 10^4 J m^{-3}$ ), and  $V$  = volume. Generally, Néel relaxation dominates at higher frequencies and in smaller NPs, and Brownian relaxation at lower frequencies in larger particles [20].

Bordelon et al. also provide SPL data for nanomag-D-spio<sup>®</sup> mNPs (MicroMod, Partikeltechnologie, GmbH, Rostock, Germany). These mNPs consist of multiple crystals of 10–12 nm diameter  $Fe_3O_4$  diffusely suspended in a dextran matrix and are also nominally 100 nm in hydraulic diameter suspended in water—the particle iron concentration was 6 ( $mg ml^{-1}$ ) [14]. Comparing Fig. 3(a) with Fig. 2(a), the SPIO particles heat much more slowly than the BNF particles, but realize much higher SPL values owing to the lower iron oxide mass in the SPIO particles. The effective imaginary relative permeability is much higher in

this material (Fig. 3(c)), but the net effect is less heating per particle in an applied magnetic field due, presumably, to the smaller amount of  $Fe_3O_4$  in each particle.

The equivalent value for  $Q_{gen}$  can be estimated from the expected iron oxide concentrations. On a per-particle basis, the BNF particles consist of a 44 nm diameter magnetite ( $Fe_3O_4$ ) core surrounded by a 32 nm thick starch shell. The density of magnetite  $\approx 5175 (kg m^{-3})$ , and for an approximate  $44.6 \times 10^{-24} (m^3)$  volume in a single BNF particle the estimate is  $2.3 \times 10^{-16} (g_{Fe})$  in the form of magnetite. At a typical small volume regional hyperthermia treatment low-end magnetic field of 24 ( $kA_{rms} m^{-1}$ , peak-to-peak)—300 Oe—as used in the mouse flank tumor experiments [5], where the SPL = 78 ( $W g_{Fe}^{-1}$ ) for BNF-Starch, we estimate a total NP power of  $17.9 \times 10^{-15} (W)$ . In a total nanoparticle of volume  $660 \times 10^{-24} (m^3)$ , including the starch coating, this would be equivalent to  $Q_{gen} = 27.6 \times 10^6 (W m^{-3})$  in the coated particle. A single nanomag-D-spio particle at the same H-field would have  $5.95 \times 10^{-18} (g_{Fe})$ , and at SPL = 88 ( $W g_{Fe}^{-1}$ ) the total NP power would be  $0.524 \times 10^{-15} (W)$ , resulting in an equivalent  $Q_{gen} = 0.794 \times 10^6 (W m^{-3})$  for a coated particle, much less than for the BNF particle in the same field. These observations agree well with the measurements and calculations of Etheridge and Bischof [13] in similar magnetic nanoparticle materials. This applied H-field is one half of the upper end of practically achievable H-fields in a mouse tumor preparation, about  $48 kA m^{-1}$  (600 Oe) in our apparatus.

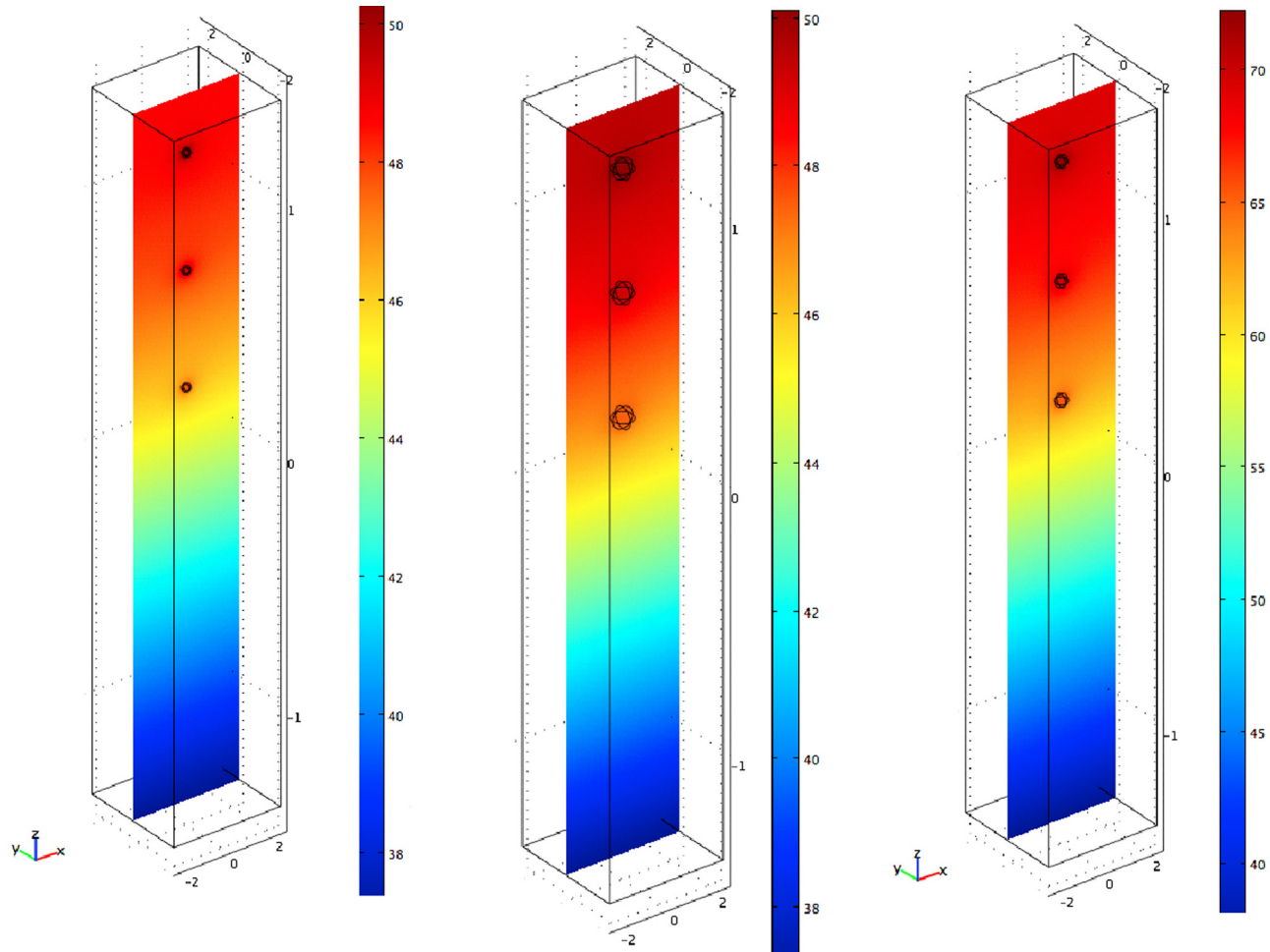


**Fig. 5 Dispersed uncoated nanoparticle numerical model results for three uniformly distributed particles, particle temperature =  $T_p$ . The distance to the isothermal bottom surface is  $1.5 \mu m$ . (a) 36 nm diameter at  $Q_{gen} = 10^{16} (W m^{-3})$  within the NP,  $T_p = 52^\circ C$  (scale  $37^\circ C$  to  $52^\circ C$ ) (b) 50 nm at  $Q_{gen} = 10^{16}$ ,  $T_p = 72^\circ C$  (scale to  $72^\circ C$ ), and (c) 80 nm at  $Q_{gen} = 10^{15}$ ,  $T_p = 50^\circ C$  (scale to  $50^\circ C$ ). Figure 5 originally appeared in Ref. [21].**

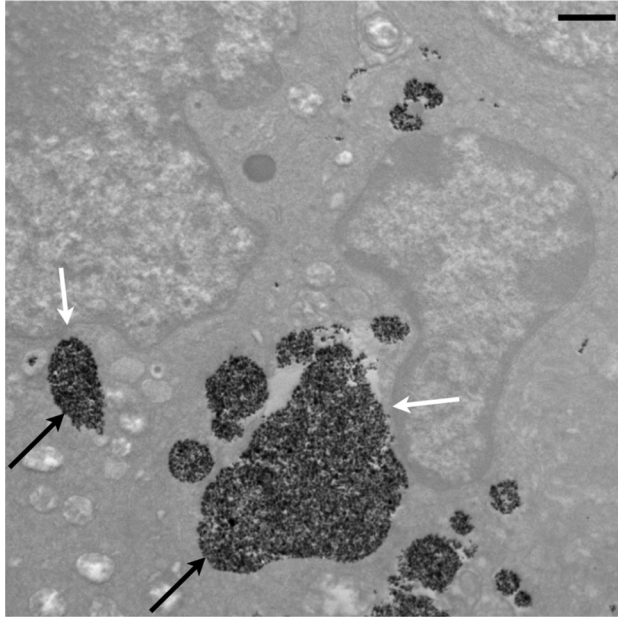


**Fig. 6** In vivo transmission electron micrograph of intracellular BNF-starch-coated iron oxide magnetic nanoparticles (black arrows) adjacent to the nuclear envelopes (white arrows) of murine breast adenocarcinoma cells. This image was taken three hours after an intra-tumoral injection of nanoparticles at a concentration of  $2.5 \text{ mg Fe/cm}^3$  tumor. The scale bar in the top right is  $1 \mu\text{m}$ . The larger particle cluster is approximately  $2 \mu\text{m}$  in effective (hydrodynamic) radius.

The super-paramagnetic iron oxide nanoparticles are said to have a heating advantage at lower magnetic field strengths [14]. However, if the same calculation is made at an applied H-field of  $4 \text{ (kA}_{\text{rms}} \text{ m}^{-1}, \text{ peak-to-peak})$ , where  $\text{SPL} = 0.26 \text{ (W g}_{\text{Fe}}^{-1})$  in the BNF particles, and  $6 \text{ (W g}_{\text{Fe}}^{-1})$  in the nanomag-D-sprio particles, then the  $Q_{\text{gen}}$  estimates still very slightly favor the BNF particles:  $90.6 \times 10^3 \text{ (W m}^{-3})$  in the BNF particles, and  $54 \times 10^3 \text{ (W m}^{-3})$  in the D-sprio particles.

**2.3 Heat Transfer Effects in Dispersed Nanoparticles.** In a landmark paper from 2002, Rabin [11] argues convincingly that dispersed nanoparticles have such short thermal time constants and are of such small volume compared to the surrounding cell

that it is unlikely that sufficient heating can be obtained to achieve hyperthermia target temperatures, approximately a  $6^\circ\text{C}$  rise above the steady state to  $43^\circ\text{C}$ . To illustrate, assume a spherical nanoparticle dispersed such that, for all practical purposes, the surroundings at  $37^\circ\text{C}$  represent an infinity boundary condition. For a spherical particle of radius,  $a$ , and assumed boundary temperature,  $T(a) = \Theta$ , the target differential heating temperature, satisfies the 1-D steady state form of Eq. (1)

$$\rho_t c_t \frac{\partial T}{\partial t} = 0 = k_t \nabla^2 T = k_t \frac{1}{r^2} \frac{\partial}{\partial r} \left[ r^2 \frac{\partial T}{\partial r} \right] \quad (7)$$

with boundary conditions  $T(a) = \Theta$ , and  $T = 0$  at very large  $r$ . Applying the boundary conditions it can quickly be shown that

$$P_{\text{tot}} = \frac{4}{3} \pi a^3 Q_{\text{gen}} = 4 \pi a^2 k_t \left. \frac{\partial T}{\partial r} \right|_a \quad (8a)$$

or

$$Q_{\text{gen}} = \frac{3 k_t \Theta}{a^2} \quad (8b)$$

where:  $P_{\text{tot}}$  is the total power dissipated in the sphere (W). To achieve a steady state particle temperature rise of  $10^\circ\text{C}$  in a medium with  $k_t = 0.5 \text{ (W m}^{-1} \text{ K}^{-1})$  for  $a = 55 \text{ nm}$  would require a uniform volume power generation of  $Q_{\text{gen}} = 5 \times 10^{15} \text{ (W m}^{-3})$ , a very large value indeed, especially when compared to the values estimated for magnetic nanoparticle heating.

**2.4 Representative Experimental Results.** Experimental studies provide calibration and guidance for numerical model studies. Figure 4 illustrates a typical experimental result. The mouse flank tumor was injected with nanoparticles, heated for 24 min at a nominal magnetic field of  $48 \text{ (kA m}^{-1} \text{ p-p})$ , ( $600 \text{ Oe p-p}$ ). The thermal camera records surface temperatures on the (shaved) skin surface. At this magnetic field strength, we might expect a volume power density of  $2 \times 10^9 \text{ (W m}^{-3})$  in the BNF-starch® nanoparticles. The surface temperatures reach  $42^\circ\text{C}$  after about 17 min of heating.

**2.5 Numerical Model Structure.** A thermal FEM model space requires at least one constant temperature or thermal flux boundary for stability. This presents a challenge when nano-dimension spaces constitute the model geometry owing to the

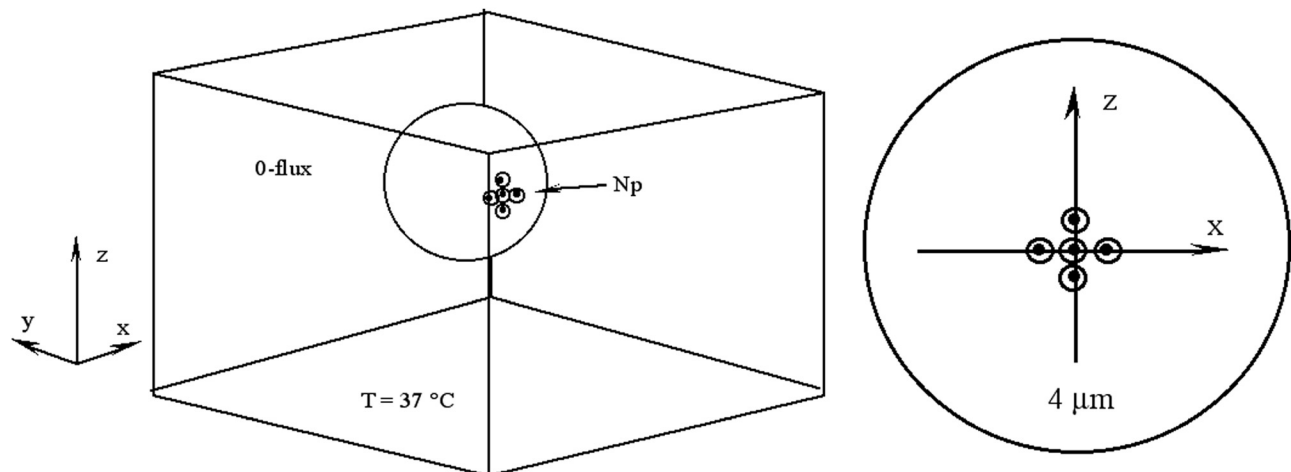


**Fig. 7** 3-D FEM model space simulating a  $10 \mu\text{m}$  cuboidal cell with  $4 \mu\text{m}$  simulated nucleus. (a) As previously, the bottom face is isothermal at  $37^\circ\text{C}$  and the other faces are 0-flux. (b) Close up view of dextran coated nanoparticle placement (not to scale). Figure 7 originally appeared in Ref. [22].



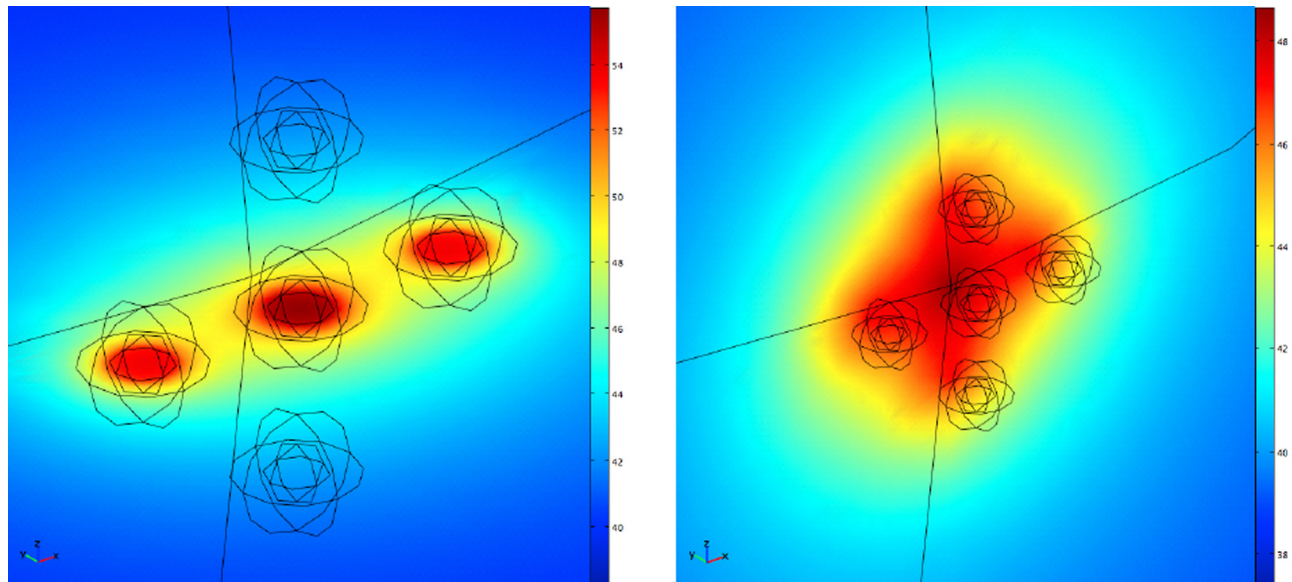


Fig. 8 3-D FEM model results at an applied volume power density  $Q_{\text{gen}} = 3 \times 10^{16} \text{ (W m}^{-3}\text{)}$  and  $t = 10 \text{ min}$ . (a) Horizontal  $X$ - $Y$  plane through the nanoparticles at the level corresponding to  $Z = 0$  in Fig. 7(b), color scale  $37^\circ\text{C}$  to  $55^\circ\text{C}$  and the particle temperature is  $55^\circ\text{C}$ . This display plane only intersects the three particles in the center of the cluster. (b) Vertical  $X$ - $Z$  plane just behind the nanoparticles at the surface of the simulated nucleus, color scale  $37^\circ\text{C}$  to  $48^\circ\text{C}$ . Figure 8 originally appeared in Ref. [22].

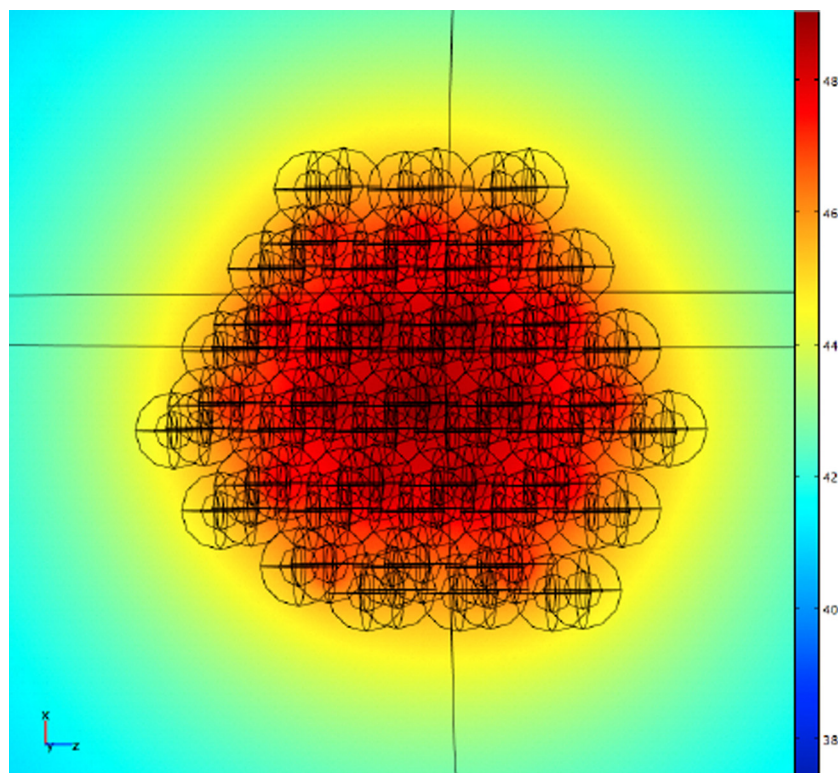


Fig. 9 A cluster of 45 dextran coated magnetic NPs of 50 nm diameter in two layers, viewed from above, at a uniform mNP volume power density of  $Q_{\text{gen}} = 3 \times 10^{15} \text{ (W m}^{-3}\text{)}$ ,  $T_{\text{max}} = 44^\circ\text{C}$ . The NP cluster measures approximately  $720 \times 620 \text{ nm}$ . The display plane is an  $X$ - $Z$  plane through the top layer of nanoparticles (the layer exposed to the cytosol). The  $43^\circ\text{C}$  contour extends to a radius of approximately 208 nm, i.e., it remains within the NP cluster dimensions.

strong heat transfer effects due to proximity of the boundaries. In the following thermal numerical models, a constant temperature boundary simulating proximity to isothermal unheated tissue was placed several microns away from the nanoparticle heat sources.

The thermal properties used in the finite element method model series are summarized in Table 1.

The numerical model series consisted of: (1) dispersed nanoparticles, (2) nanoparticle clusters in a single cell, and (3) a geometric



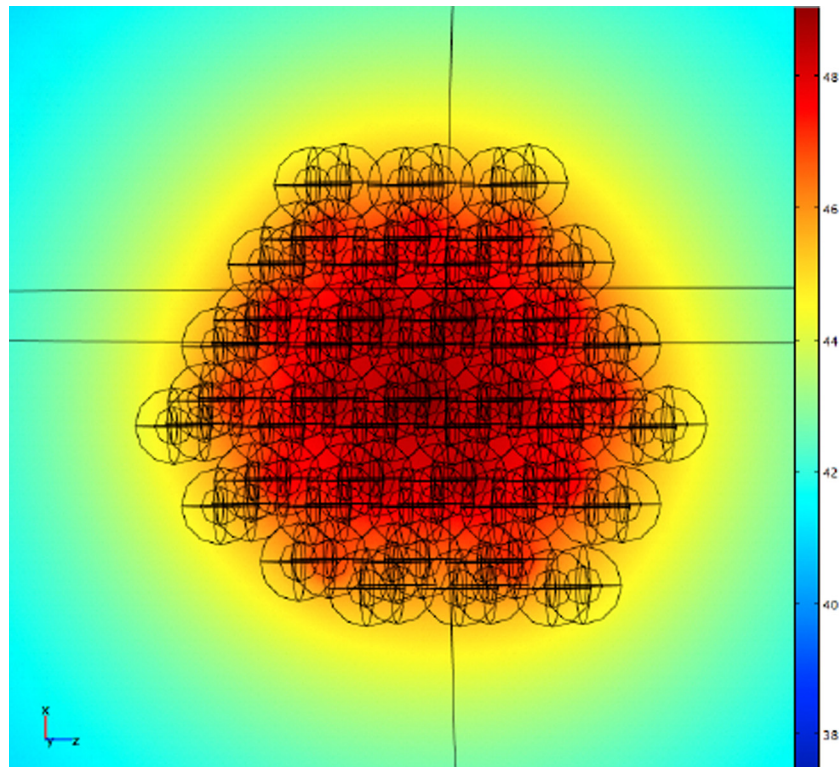


**Fig. 10** A cluster of 90 dextran coated magnetic NPs of 50 nm diameter in four layers at a volume power density of  $Q_{\text{gen}} = 3 \times 10^{15} \text{ (W m}^{-3}\text{)}$ ,  $T_{\text{max}} = 49^\circ\text{C}$ . The coated NP cluster measures approximately  $750 \times 650 \text{ nm} \times 500 \text{ nm}$  tall. The display plane is an  $X$ - $Z$  plane through the same layer of nanoparticles as in Fig. 8 (this layer is now an interior layer). The  $43^\circ\text{C}$  contour extends to a radius of approximately 450 nm ( $\sim 200 \text{ nm}$  to  $300 \text{ nm}$  outside of the cluster).

approximation to nanoparticle clusters employing equivalent ellipsoidal volumes that makes larger scale multiple cell models with multiple nanoparticle clusters practical (Table 2).

### 3 Results

The goal of the numerical model series was to determine the conditions required to achieve hyperthermic range temperatures in a realistically sized tumor. At a typical reported experimental maximum applied magnetic field,  $2.79 \times 10^4 \text{ (A m}^{-1}\text{)}$  peak-to-peak—i.e., 350 Oe—in BNF-Starch nanoparticles at a frequency of 150 kHz, we should be able to achieve  $Q_{\text{gen}} \approx 6.9 \times 10^8 \text{ (W m}^{-3}\text{)}$ , assuming a relative imaginary permeability,  $\mu''_r = 6$  (as in Fig. 2(c)), many orders of magnitude below the analytical estimation of Eq. (8). The numerical models confirm the analytical prediction. Clustering of the particles improves the heating, but the small clusters used in the example models are not able to adequately mimic the much larger clusters typical in the experiments.

**3.1 Dispersed Nanoparticles.** The trends expected from the analytical considerations are borne out in the numerical models. Dispersed nanoparticles require extreme local volume power densities to achieve therapeutic temperatures and reach steady state typically within a few ms in the small geometries considered. The first series of calculations include uncoated magnetically heated nanoparticles at a nominal uniform distribution,  $1 \times 10^{13} \text{ (Np ml}^{-1}\text{)}$ . The dispersed single particle results, Fig. 5, simulate three particles separated by 464 nm (the uniform dispersion) and located  $1.5 \mu\text{m}$  from an isothermal (bottom) surface at  $37^\circ\text{C}$ . The top surface is a thermally insulated boundary (plane of symmetry) simulating adjacent unheated isothermal tissues that are  $6 \mu\text{m}$  apart. In these models, extreme volume power densities,  $10^{16}$

$\text{(W m}^{-3}\text{)}$ , are required to achieve a measurable temperature rise in the smaller particles, decreasing as the particle size increases. We note that a uniform dispersion of  $10^{13} \text{ (NP ml}^{-1}\text{)}$  equates to approximately 10,000 NPs in a cuboidal cell  $10 \mu\text{m}$  on a side.

**3.2 Clustered Nanoparticles.** The magnetic field must be very high to achieve adequate heating in nanoparticle groups. Experiments typically require tens of kW of 150–160 kHz current resulting in magnetic field strengths of  $8 \text{ kA m}^{-1}$  to  $28 \text{ kA m}^{-1}$  (100 Oe to 350 Oe) to heat iron oxide nanoparticles *in vivo*—i.e., to couple mW of heating into the tissues [5,6]. This maximum is near the lower end of the minimum treatment magnetic field strengths suggested by Etheridge and Bischof [13]. And yet, adequate heating can be achieved.

Recent results indicate that absorbed intracellular coated nanoparticles are clustered into cytoplasmic endosomes, as in Fig. 6 [5]. Clustering of the particles significantly reduces the power densities required to achieve therapeutic temperatures for specific ferromagnetic NPs. The BNF-Starch nanoparticles illustrated are nominally 100 nm in diameter with a 25 nm dextran coating, and from the electron micrograph an estimated hydrodynamic cluster radius is approximately  $2 \mu\text{m}$ . If we assume that the dextran coating is not disturbed, and if the cluster in Fig. 6 were a sphere, it would contain approximately 18,965 mNPs, with volume fractions of 30%  $\text{Fe}_3\text{O}_4$  and 70% dextran. At the reported magnetic field strength of the experiment in Fig. 4,  $17 \times 10^3 \text{ (A m}^{-1}\text{ rms)}$  and  $Q_{\text{gen}} = 2 \times 10^9 \text{ (W m}^{-3}\text{)}$ , a single cluster of that size would couple 20 nW to the cell ( $\mu''_r = 6$  and  $f = 150 \text{ kHz}$ ) for an average cell volume power of  $Q_{\text{v-avg}} = 20 \times 10^6 \text{ (W m}^{-3}\text{)}$  in an assumed cuboidal cell  $10 \mu\text{m}$  on a side. By Eq. (8b) an equivalent single spherical cell volume with one such mNP cluster surrounded by unheated tissue would have a temperature rise of 0.43 mK at the

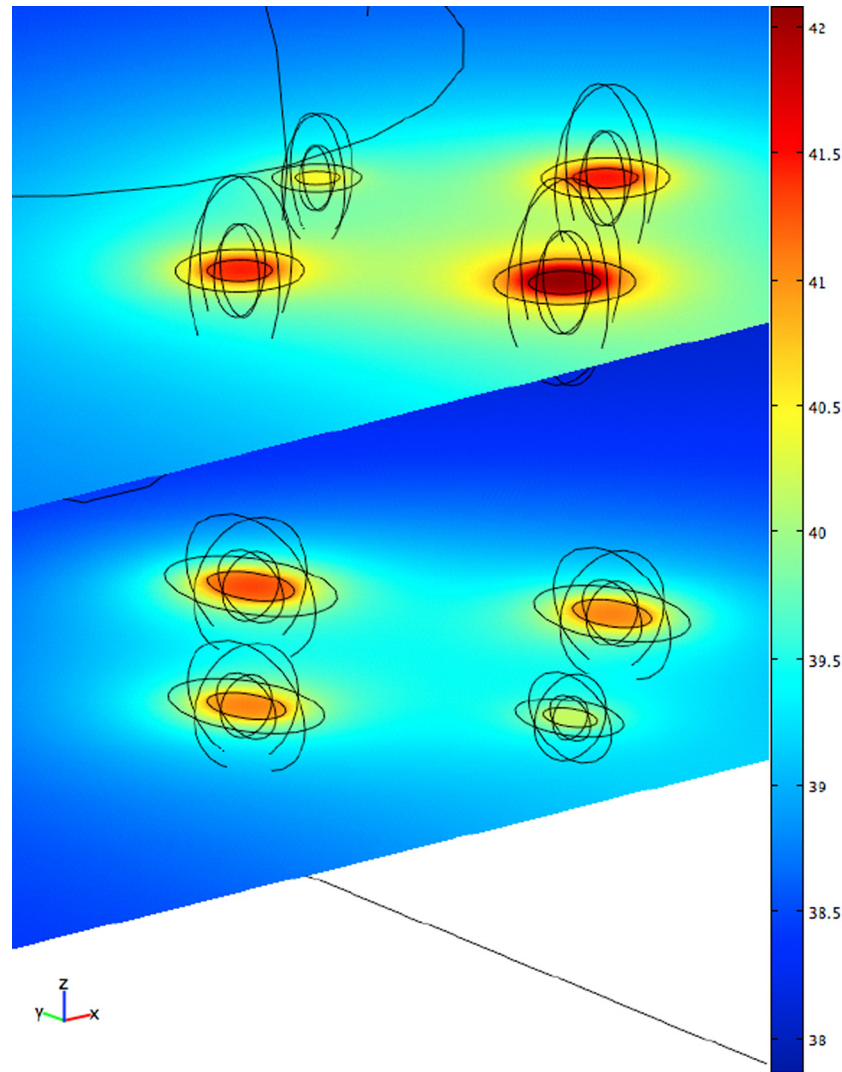


**Fig. 11** Eight prolate ellipsoids in 2 X-Y planes with equivalent volumes of 90 (2 ea.), 270 (4 ea.), and 360 (2 ea.) magnetic NPs of 50 nm diameter with dextran coating at a volume power density of  $Q_{\text{gen}} = 1.5 \times 10^{14} \text{ (W m}^{-3}\text{)}$  has  $T_{\text{max}} = 42^\circ\text{C}$ . The model space simulates a total of 1980 NPs. The total coupled power is 19.5 mW, virtually the same as for the single ellipsoid in Fig. 11. The display planes are X-Y through the centers of the ellipsoids.

experimental magnetic field. Single cell heating does not provide therapeutic results.

**3.2.1 Magnetic Nanoparticles.** The 3-D model space used is depicted in Fig. 7. In the initial model, five 50 nm diameter magnetic nanoparticles with 25 nm thick dextran coatings were placed on the nuclear surface, as shown (exaggerated relative dimensions in the figure). The nanoparticle cluster has an effective hydrodynamic diameter of approximately 86 nm not including the dextran coating, much smaller than the cluster in Fig. 6.

An applied volume power density of  $3 \times 10^{16} \text{ (W m}^{-3}\text{)}$  was required to achieve a nanoparticle temperature of  $55^\circ\text{C}$  (Fig. 8). In the figure, the highly localized nature of the heating is apparent, with the elevated temperature zone confined to within a few diameters of the nanoparticles.

In this case, the applied volume power density is three times that in the dispersed model of Fig. 5(b); however, the heat transfer volume in the model of Fig. 8 is orders of magnitude larger in dimension. This illustrates the importance of local heat transfer effects on the result.

When the nanoparticle cluster was adjusted to a more densely packed equilateral hexagonal array separated by 120 nm on center

and approximately tripled to 19 nanoparticles a steady state particle temperature of  $50^\circ\text{C}$  was reached at  $Q_{\text{gen}} = 1 \times 10^{16} \text{ (W m}^{-3}\text{)}$  in less than 1 s. The 20 nm gap between particles was necessary to prevent singularities and inverted elements when meshing the geometry. Further increasing the cluster to 45 nanoparticles in two equilaterally separated layers (pyramidal NP geometry, Fig. 9) the particle temperature reached  $44^\circ\text{C}$  at  $Q_{\text{gen}} = 3 \times 10^{15} \text{ (W m}^{-3}\text{)}$  in less than 0.1 s. Figure 9 is an X-Z plane slice through the top layer of nanoparticles for that numerical model. Note in the figure that the exterior nanoparticles show very little steady state temperature rise relative to the interior nanoparticles, and apparently act mostly to reduce heat transfer losses from the interior particles.

The two nanoparticle layers are shielded from horizontal (lateral) heat transfer effects, but not from 1-D vertical heat transfer, which accounts for the lack of increased heating. Similar results were obtained when a two-layer 180 NP cluster was created (i.e., the same cluster thickness with extended lateral dimensions)—the maximum temperature at  $Q_{\text{gen}} = 1 \times 10^{15} \text{ (W m}^{-3}\text{)}$  was  $42^\circ\text{C}$ , confirming that the horizontal extension of thin NP clusters alone does not improve heating characteristics appreciably. Expanding the cluster to 90 NPs by stacking 45

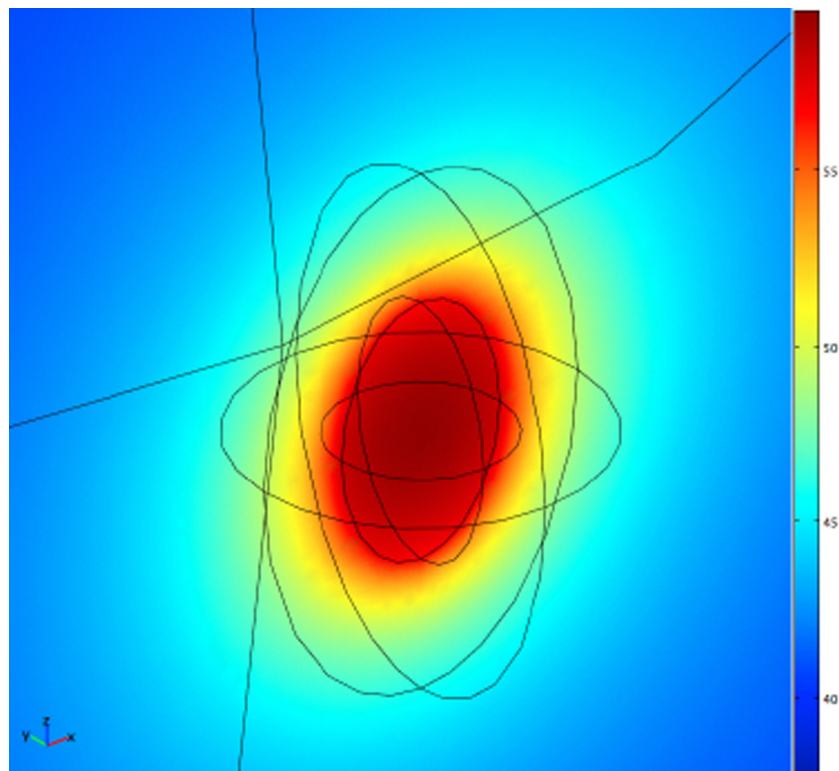


**Fig. 12** A single prolate ellipsoid with equivalent volume to the 90 magnetic NPs of 50 nm diameter with dextran coating at a volume power density of  $Q_{\text{gen}} = 3 \times 10^{15}$  ( $\text{W m}^{-3}$ ) has  $T_{\text{max}} = 59.5^\circ\text{C}$ . The coated NP ellipsoid measures approximately  $391 \times 391 \text{ nm} \times 586 \text{ nm}$  tall. The display plane is an X-Z plane through the center of the ellipsoids. The  $43^\circ\text{C}$  contour extends to an X-semi-axis of approximately 356 nm ( $\sim 160 \text{ nm}$  outside of the dextran ellipsoid).

additional NPs in two layers vertically, yielding a 4-layer stack  $1.1 \mu\text{m}$  thick (and approximately  $650 \times 750 \text{ nm}$  in width and length), alters the cluster heat transfer boundary conditions so that  $Q_{\text{gen}} = 3 \times 10^{15}$  ( $\text{W m}^{-3}$ ) results in middle layer temperatures of  $49^\circ\text{C}$ , as in Fig. 10, (compare to  $44^\circ\text{C}$  for the 45 NP two-layer stack).

However, these models are still many orders of magnitude from the ability to represent practically achievable magnetic field heating, and the modeling problem has grown to unwieldy geometric proportions. The detailed multiple nanoparticle model space is computationally intensive: the 90 NP cluster model consisted of almost 200 subdomains, meshed out to 133,679 elements ( $\sim 98$  elements per magnetic sphere and 304 per dextran sphere), resulting in 181,023 degrees of freedom in the solution. The 90 NP model of Fig. 10 coupled a total power of  $17.7 \mu\text{W}$  into the cell. This NP cluster is very small compared to the endosome in Fig. 6, but a detailed geometric model of a 81,000 NP cluster is a formidable task. Additionally, the numerical model results suggest that a single cluster in a cell is not an effective source of heating power because it reaches steady state temperatures in extremely short times (less than a second) and will not “bloom” to heat the entire cell if one side is isothermal at body temperature.

It would be extremely useful to be able to apply a lower-order engineering design approximation to estimate heating effectiveness when there are multiple intracellular clusters of differing numbers of NPs. If it can be reasonably assumed that a closely packed nanoparticle cluster operates analogously to a lumped aggregate, a first approximation in a substantially simpler geometric model space is to assume that a single aggregate particle with the same volume of magnetic material can be used to simulate a nanoparticle cluster in an equivalent thermal sense, at least. Such an ellipsoid with the equivalent volume of dextran coating was

placed at the same location in the cell. For this equivalent magnetic NP ellipsoid, the X- and Y-semi-axes are 98 nm and the Z-semi-axis is 147 nm (aspect ratio 1.5). At the same volume generation power,  $3 \times 10^{15}$  ( $\text{W m}^{-3}$ ), the ellipsoid-center temperature reaches  $59.5^\circ\text{C}$ , at steady state (in less than 0.2 s),  $10^\circ\text{C}$  higher than the individual NPs in Fig. 10; however, the  $43^\circ\text{C}$  contour outside of the ellipsoid compares very favorably with the individual NP result of Fig. 10. Incidentally, the ellipsoid-center heating pattern blooms only very slightly between 0.2 and 30 s, and not at all thereafter. So, while the center temperature will be over-estimated, the heating effectiveness at distance ought to be represented with acceptable accuracy. The heating distribution is still quite disappointing, however, due to the intense vertical thermal gradients.

A multiple ellipsoid model illustrates the advantage gained by several spatially distributed nanoparticle clusters. Three ellipsoids were added to the nucleus center plane, two with scaled volumes equivalent to 270 nanoparticles (at lateral locations in Fig. 11), and one with scaled volume equivalent to 360 nanoparticles (farthest from the cell nucleus), and the ellipsoids are separated by approximately  $2 \mu\text{m}$  in the X-Y plane. An additional layer with 4 NP cluster ellipsoids was added  $2 \mu\text{m}$  below the nucleus center layer (equivalent to a total of 1980 simulated NPs in the cell). Applying essentially the same total power as in the single ellipsoid case of Fig. 12— $19.5 \mu\text{W}$  in this case ( $Q_{\text{gen}} = 1.5 \times 10^{14} \text{ W m}^{-3}$ ) compared to  $17.7 \mu\text{W}$  in the previous model—results in slightly lower center temperatures ( $45^\circ\text{C}$  in the largest ellipsoids in Fig. 11), but a small bloom in the spatial temperature distributions between the ellipsoids, in-plane.

This suggests that effective heating in vivo with a spatial temperature distribution that develops over multiple minutes might depend on achieving a nanoparticle uptake by the cells of many



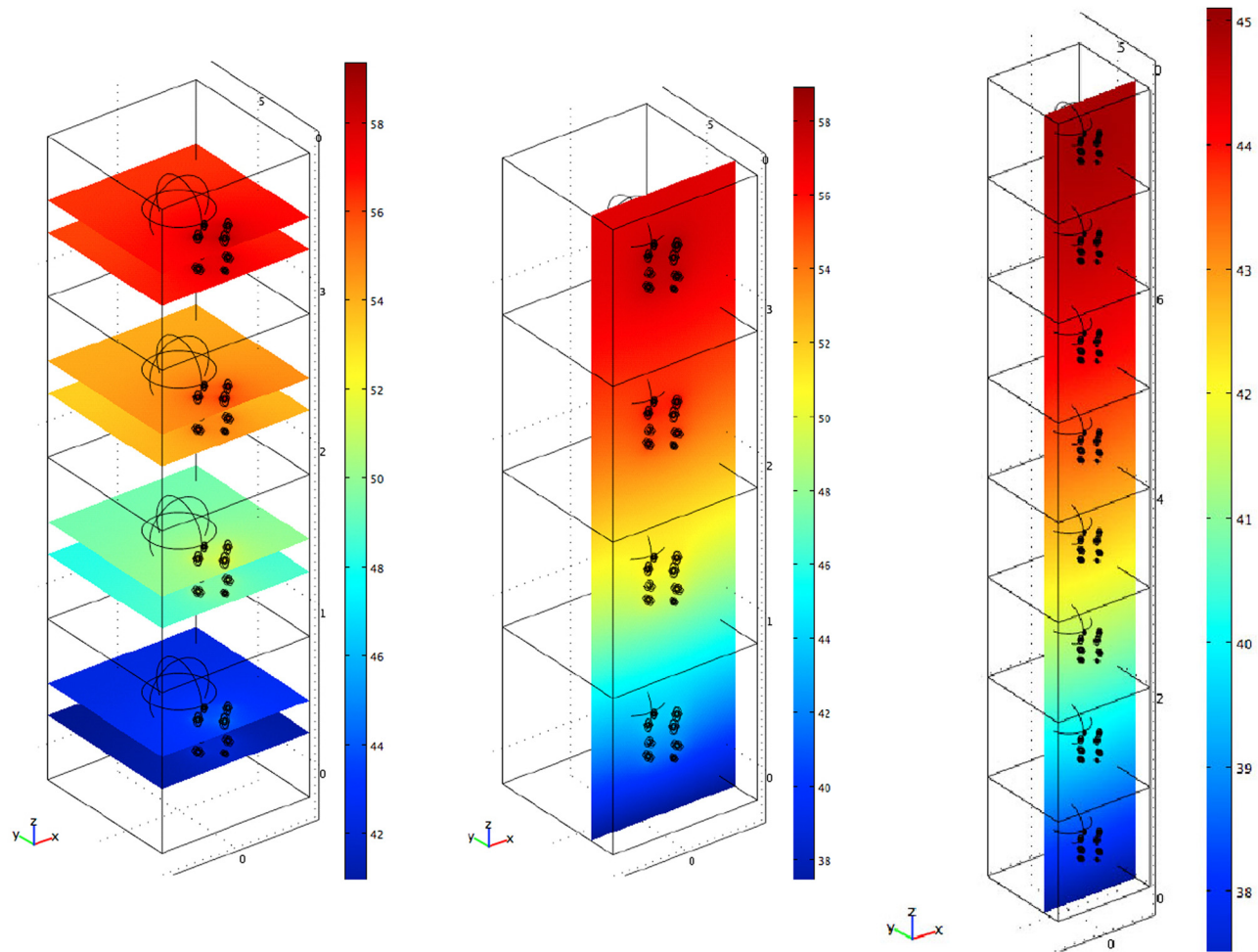


**Fig. 13** Four cells stacked vertically, each with eight prolate ellipsoids, as in Fig. 12. The applied volume power density has been reduced to  $Q_{\text{gen}} = 1 \times 10^{14}$  ( $\text{W m}^{-3}$ ) resulting in  $T_{\text{max}} = 59^\circ\text{C}$  in the uppermost cell. The total coupled power is  $13 \mu\text{W}$  per cell. (a) Eight X-Y display planes through the centers of the ellipsoids. (b) A single X-Z plane through the central pair of ellipsoids. (c) Eight cell model each with duplicate NP distributions, a total of 15,840 NPs heated with  $Q_{\text{gen}} = 1 \times 10^{13}$  ( $\text{W m}^{-3}$ ) reaches a steady state temperature of  $45^\circ\text{C}$  in less than 1 s.

clusters of at least several hundred nanoparticles each in relatively close proximity—or more likely thousands of NPs. But, more than that, the local heat transfer to the isothermal surface prevents any longer term expansion of the heating pattern, which is more disturbing. It is not hard to understand why that is: the 0-flux side and top planes of the cell simulate a  $20 \mu\text{m}$  thick slab of heated tissue between isothermal boundaries, a very thermally thin slab indeed.

To study the effect of the overall tissue thickness, an additional model of four such cells vertically stacked were heated, each with a total coupled power of  $13 \mu\text{W}$ ,  $Q_{\text{gen}}$  reduced to  $1 \times 10^{14}$  ( $\text{W m}^{-3}$ ). This is equivalent to a heated tissue thickness of  $80 \mu\text{m}$  between isothermal tissue boundaries. The four cells simulate a total of 7920 NPs. The lowermost cell continues to show very disappointing heating with negligible lateral spread in the pattern, but does act as a thermal shield to enhance heating in the upper cells. The uppermost cell heats relatively uniformly to a temperature near  $59^\circ\text{C}$ , a much more acceptable result. The thermal shielding of the lower layers of cells effectively neutralizes the strong vertical temperature gradients, enabling the lateral pattern to develop above the second cell in this model (Fig. 13).

The model space must be significantly expanded to better represent the experiment geometry. In a third series of models, a single ellipsoidal NP cluster of 81,000 NPs with  $100 \text{ nm}$  diameter  $\text{Fe}_3\text{O}_4$  central magnetic material surrounded by 25 shells of dextran, similar to the experimental measurement in Fig. 6 (assuming four

such clusters of NPs), was placed in the vicinity of the nucleus. The resulting equivalent coated NP cluster measured  $5.64 \times 5.64 \times 8.46 \mu\text{m}$  elliptical diameters (aspect ratio 1.5, as in the earlier models).

In the first calculation, Fig. 14(a), a single heated cell was located above four unheated neighbors with a lower isothermal  $37^\circ\text{C}$  surface. A steady state NP temperature of  $48.6^\circ\text{C}$  was reached in about 0.1 s at an applied  $Q_{\text{gen}} = 3 \times 10^{11}$  ( $\text{W m}^{-3}$ ) in the iron oxide, and the significant heat transfer to the adjacent unheated cells is easily seen in the plot. In Fig. 14(b), four heated cells with the same NP load reached  $42.8^\circ\text{C}$  at  $Q_{\text{gen}} = 3 \times 10^{10}$  ( $\text{W m}^{-3}$ ).

The simulated distance between isothermal surfaces is  $160 \mu\text{m}$  in this geometry. The required volume power density is still about an order of magnitude above the maximum practical experimental value, but the trend toward achievable levels is clear.

## 4 Discussion

The typical cgs unit system used to describe magnetic nanoparticle heating presents some philosophical difficulties that are resolved by the use of SI units, and are to be preferred. The cardinal physical property in this case is the effective value of the imaginary part of the permeability,  $\mu''$  ( $\text{Hy m}^{-1}$ ), and conversion of results from typical literature format to this form has been described. Both the hysteresis loop and super-paramagnetic

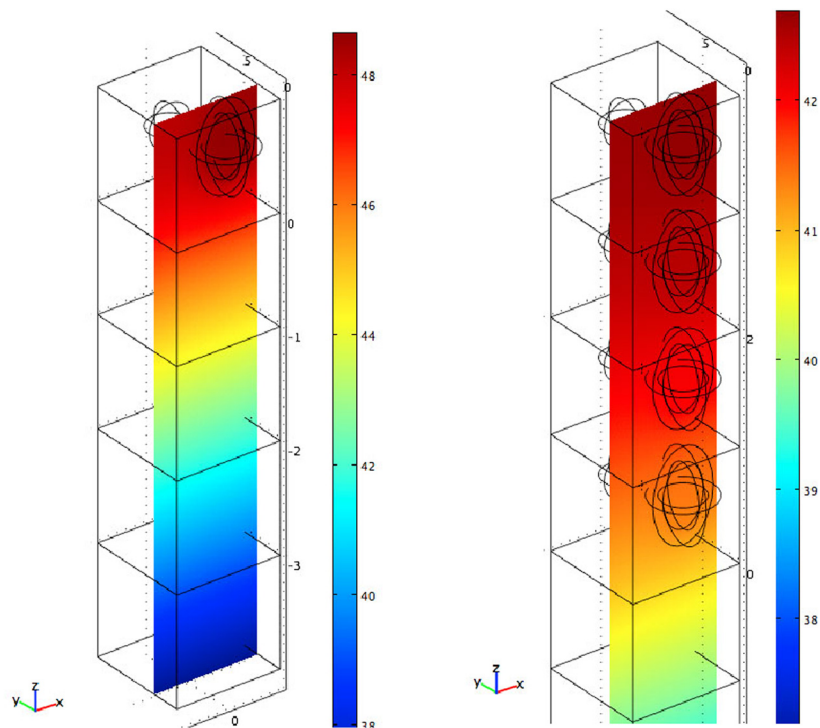


**Fig. 14** (a) A single heated cell containing a single 81,000 mNP cluster with four unheated neighbor cells. NP  $Q_{\text{gen}} = 3 \times 10^{11} \text{ (W m}^{-3}\text{)}$  in the model. The X-Z display plane is through the center of the ellipsoidal NP cluster. Note the volume of the NP cluster relative to the nucleus and cell volumes. The steady state temperature distribution was reached in 0.1 s. (b) X-Z display plane for four similarly loaded cells (81,000 NPs each) with four unheated neighbors (not shown) at  $Q_{\text{gen}} = 3 \times 10^{10} \text{ (W m}^{-3}\text{)}$ . Again, steady state was reached at about  $t = 0.15 \text{ s}$ .

magnetic particles in this work exhibit complex nonlinear behavior since  $\mu''$  is a function of the applied magnetic field.

The numerical model results illustrate the importance of nanoparticle clustering to achieve adequate heating. The volume power generation required to achieve therapeutic temperature ranges decreases dramatically as the distance between unheated isothermal surfaces increases. While the model spaces in this study are not sufficiently large to observe heating at experimentally applied H-fields, the trend toward more easily achievable  $Q_{\text{gen}}$  is clear in the larger model spaces and larger NP clusters. Plainly, local heat transfer is a dominant mechanism. In fact, the spherical equivalent to a single  $10 \mu\text{m}$  cuboidal cell (volume  $= 1 \times 10^{-15} \text{ m}^3$ ) composed entirely of the dextran coated nanoparticles (565,000 NPs) as used in the numerical models at the estimated experimental  $Q_{\text{gen}} = 2 \times 10^9 \text{ (W m}^{-3}\text{)}$  in the iron oxide (30% of the cell volume) would couple a total of  $0.6 \mu\text{W}$  to the single cell. In surrounding unheated medium, the cell would have a steady state temperature rise of only  $0.013^\circ\text{C}$  by Eq. (8b). Also by Eq. (8b), a single completely packed dextran coated NP sphere would have to have a radius of  $173 \mu\text{m}$  to achieve a temperature rise of  $10^\circ\text{C}$  at the experimental iron oxide volume power density, much larger than most cells. Single cell heating cannot be adequate to achieve therapeutic temperatures even at very high magnetic field strengths [21].

The insight gained by expanding the model geometry to larger systems justifies the uncertainties introduced by the geometric simplification employed in constructing the approximate cluster models. The dominant nature of local heat transfer processes is easily seen in the results. The short times to reach steady state confirm that even the largest model geometry ( $160 \mu\text{m}$  equivalent radius) is far too small to simulate experimental work. This supports the suggestion of Etheridge and Bischof that the minimum

treatable tumor size with this modality is likely to be about 2 mm in radius [13], and Hedayati et al. also suggest a minimum treatable volume of  $1 \text{ mm}^3$  [8].

The upper limit of applicable magnetic field strengths is determined by the onset of significant nonspecific eddy current heating. In a mouse model at 150 kHz eddy current heating is negligible:  $Q_{\text{gen}}$  (at max  $r = 3 \text{ cm}$ ) is on the order of  $2 \times 10^3 \text{ (W m}^{-3}\text{)}$  when the applied H-field is  $24 \text{ (kA m}^{-1}\text{)}$  peak-to-peak and  $\sigma = 0.1 \text{ (S m}^{-1}\text{)}$ , a very modest induction heating rate. Etheridge and Bischof [13] also discuss this induction heating limitation based on the calculations of Atkinson et al. [22]. Induction heating increases to  $57 \times 10^3 \text{ (W m}^{-3}\text{)}$  at a representative chest radius of 15 cm at this frequency and field strength. This suggests that large whole-body solenoidal coils will likely prove impractical in large animals and humans, necessitating focused regional magnetic field heating.

It is now clear that to achieve effective tissue heating with magnetic NPs the NP construction, NP-NP association, total Fe dose ( $\text{mg ml}^{-1} \text{ tissue}$ ), NP  $Q_{\text{gen}}$ , and tissue geometry must be matched in some sense. The relationship of magnetic NP heating in tissues using those parameters is always limited by eddy current (magnetic induction) potential, which is governed by the AMF parameters.

By improving the heating characteristics of nanoparticles clustered in tumor cells the therapeutic ratio of nanoparticle-based hyperthermia treatment of tumors can be improved. At this time the exact relationship between intracellular, membrane and extracellular NP location, Fe content, thermal dose and cytotoxicity is unclear. Although significant experimentation is ongoing, the relationship between tissue biodistribution, iron content, achieved thermal dose and primary and adjuvant therapeutic effect also remains unclear. Preliminary information suggests that

magnetic NP aggregation improves primary tissue heating, but that better distribution may improve adjuvant radiation and chemotherapeutic effects.

## 5 Conclusion

The dominant importance of the local heat transfer environment on temperatures achievable in magnetic field heating of nonuniformly dispersed nanoparticles is revealed by larger volume FEM models than have appeared to date, and has been underappreciated in the wide sense. Effective temperature rise in tumors is critically dependent on biodistribution in a critical mass: the model results suggest that it is highly unlikely that effective magnetic particle heating can be achieved in tumors much less than mm dimensions. Our models also suggest that unabsorbed NPs at the tumor periphery might be helpful in providing some heat transfer shielding. The distance between unheated isothermal boundaries is just as critical a determinant of likely success as the NP load in individual cells. To date, perfusion effects have not been included. When they are, we anticipate that the predominantly capillary nature of typical tumor vasculature will act to more evenly distribute the heating. The presence of thermally significant vessels in the heating field will likely mimic the effect seen with proximal isothermal surfaces.

The clustering of iron oxide nanoparticles significantly improves the electromagnetic heating of those particles. In order to ameliorate the computational intensity of the detailed nanoparticle modeling problem, we have introduced essentially thermally equivalent solid representations of the particles, which are clustered by intrinsic cellular processes; we should expect the clustering processes to differ among cell types, adding an additional layer of complexity to model formulation. The simplified geometric approximation will undoubtedly prove useful in formulating realistic tumor scale model spaces. These results provide a common general engineering foundation for analysis and modeling in nanoparticle heating and will aid in design of nanoparticles for cancer therapy, experiment interpretation, and in treatment planning.

## Acknowledgment

This work was partially supported by the T. L. L. Temple Foundation, the O'Donnell Foundation, and by NIH NCI Grant No. 1U54CA151662-03. Hysteresis loop data for Fig. 1(b) were kindly provided by Dr. Aleta T. Wilder, of the Process Energetics Laboratory at the University of Texas at Austin.

## References

- [1] Cassim, S. M., Giustini, A. J., Petryk, A. A., Strawbridge, R. A., Hoopes, P. J., 2009, "Iron Oxide Nanoparticle Hyperthermia and Radiation Cancer Treatment," *Proc. SPIE* **7181**, Paper No. 718100.
- [2] Johannsen, M., Gneveckow, U., Eckelt, L., Feussner, A., Waldofner, N., Scholz, R., Deger, S., Wust, P., Loening, S. A., Jordan, A., 2005, "Clinical Hyperthermia of Prostate Cancer Using Magnetic Nanoparticles: Presentation of a New Interstitial Technique," *Int. J. Hyperthermia*, **21**(7), pp. 637–647.
- [3] Harris, N., Ford, M. J., Cortie, M. B., 2006, "Optimization of Plasmonic Heating by Gold Nanospheres and Nanoshells," *J. Phys. Chem. B*, **110**(22), p. 10701.
- [4] Gannon, C. J., Patra, C. R., Bhattacharya, R., Mukherjee, P., and Curley, S. A., 2008, "Intracellular Gold Nanoparticles Enhance Non-Invasive Radiofrequency Thermal Destruction of Human Gastrointestinal Cancer Cells," *J. Nanobiotechnology*, **6**, Paper No. 2.
- [5] Giustini, A. J., Gottesman, R. E., Rauwerdink, A. M., Petryk, A. A., Weaver, J. B., and Hoopes, P. J., 2011, "Kinetics and Pathogenesis of Intracellular Iron-Oxide Nanoparticle Hyperthermia," *Proc. SPIE* **7901**, Paper No. 790118.
- [6] Hoopes, P. J., Tate, J. A., Ogden, J. A., Strawbridge, R. R., Fiering, S. N., Petryk, A. A., Cassim, S. M., Giustini, A. J., Demidenko, E., Ivkov, R., Barry, S., Chinn, P., and Foreman, A., 2009, "Assessment of Intratumor Non-Antibody Directed Iron Oxide Nanoparticle Hyperthermia Cancer Therapy and Antibody Directed IONP Uptake in Murine and Human Cells," *Proc. SPIE* **7181**, Paper No. 71810P.
- [7] Dennis, C. L., Jackson, A. J., Borchers, J. A., Hoopes, P. J., Strawbridge, R., Foreman, A. R., van Lierop, J., Grüttner, C., and Ivkov, R., 2009, "Nearly Complete Regression of Tumors via Collective Behavior of Magnetic Nanoparticles in Hyperthermia," *Nanotechnology*, **20**(39), p. 395103.
- [8] Hedayati, M., Thomas, O., Abubaker-Sharif, B., Zhou, H. M., Cornejo, C., Zhang, Y., Wabler, M., Mihalic, J., Gruettner, C., Westphal, F., Geyh, A., Deweese, T. L., and Ivkov, R., 2013, "The Effect of Cell Cluster Size on Intracellular Nanoparticle-Mediated Hyperthermia: Is it Possible to Treat Microscopic Tumors?," *Nanomedicine*, **8**(1), pp. 29–41.
- [9] Gordon, R. T., Hines, J. R., and Gordon, D., 1979, "Intracellular Hyperthermia: A Biophysical Approach to Cancer Treatment via Intracellular Temperature and Biophysical Alteration," *Med. Hypotheses*, **5**, pp. 83–102.
- [10] Hilger, I., Andra, W., Bähring, R., Daum, A., Hergt, R., and Kaiser, W. A., 1997, "Evaluation of Temperature Increase With Different Amounts of Magnetite in Liver Tissue Samples," *Invest. Radiol.*, **32**(11), pp. 705–712.
- [11] Rabin, Y., 2002, "Is Intracellular Hyperthermia Superior to Extracellular Hyperthermia in the Thermal Sense?," *Int. J. Hyperthermia*, **18**(3), pp. 194–202.
- [12] Giustini, A. J., Ivkov, R., and Hoopes, P. J., 2011, "Magnetic Nanoparticle Biodistribution Following Intratumoral Administration," *Nanotechnology*, **22**(34), p. 345101.
- [13] Etheridge, M. L., and Bischof, J. C., 2013, "Optimizing Magnetic Nanoparticle Based Thermal Therapies Within the Physical Limits of Heating," *Ann. Biomed. Eng.*, **41**(1), pp. 78–88.
- [14] Bordonon, D. E., Cornejo, C., Grüttner, C., Westphal, F., Deweese, T. L., and Ivkov, R., 2011, "Magnetic Nanoparticle Heating Efficiency Reveals Magneto-Structural Differences When Characterized With Wide Ranging and High Amplitude Alternating Magnetic Fields," *J. Appl. Phys.*, **109**(12), p. 124904.
- [15] Brosseau, C., Youssef, J. B., Talbot, P., and Konn, A.-M., 2003, "Electromagnetic and Magnetic Properties of Multicomponent Metal Oxides Heterostructures: Nanometer Versus Micrometer-Sized Particles," *J. Appl. Phys.*, **93**(11), pp. 9243–9256.
- [16] Dennis, C. L., Jackson, A. J., Borchers, J. A., Ivkov, R., Foreman, A. R., Lau, J. W., Goernitz, E., and Gruettner, C., 2008, "The Influence of Collective Behavior of the Magnetic and Heating Properties of Iron Oxide Nanoparticles," *J. Appl. Phys.*, **103**(7), p. 07A319.
- [17] Hergt, R., Andra, W., d'Ambly, C. G., Hilger, I., Kaiser, W. A., Richter, U., and Schmidt, H. G., 1998, "Physical Limits of Hyperthermia Using Magnetite Fine Particles," *IEEE Trans. Magn.*, **34**(5), pp. 3745–3754.
- [18] Baker, I., Zeng, Q., Li, W., and Sullivan, C. R., 2006, "Heat Deposition in Iron Oxide and Iron Nanoparticles for Localized Hyperthermia," *J. Appl. Phys.*, **99**(8), p. 08H106.
- [19] Rosensweig, R. E., 2002, "Heating Magnetic Fluid With Alternating Magnetic Field," *J. Magn. Magn. Mater.*, **252**, pp. 370–374.
- [20] Hergt, R., Dutz, S., and Zeisberger, M., 2010, "Validity Limits of the Néel Relaxation Model of Magnetic Nanoparticles for Hyperthermia," *Nanotechnology*, **21**, p. 015706.
- [21] Pearce, J. A., 2011, "FEM Numerical Model Study of Heating in Magnetic Nanoparticles," *Proc. SPIE* **7901**, Paper No. 790110.
- [22] Atkinson, W. J., Brezovich, I. A., and Chakraborty, D. P., 1984, "Usable Frequencies in Hyperthermia With Thermal Seeds," *IEEE Trans. Biomed. Eng.*, **31**(1), pp. 70–75.